Check for updates

ADVANCED MATERIALS INTERFACES
www.advmatinterfaces.de

Stable Manganese-Oxide Composites as Cathodes for Zn-Ion Batteries: Interface Activation from In Situ Layer Electrochemical Deposition under 2 V

*Inmaculada Álvarez-Serrano, Paloma Almodóvar, David Agustín Giraldo, Francisco Llopis, Benjamín Solsona, and María Luisa López**

A set of multiphase manganese-oxide composite materials (Mn_2O_3@Mn_3O_4 and Mn_3O_4@Mn_5O_8), and a birnessite-type K_xMnO_2 oxide are prepared and evaluated as cathodes for Zn-ion batteries. The species formed when the electrodes are subjected to 2 V in aqueous solutions of $MnSO_4$ and $ZnSO_4$ are analyzed, suggesting an interphase activation leading to enhancement of electrochemical response. For the first time, it is shown that a $Zn_4(SO_4)(OH)_6.xH_2O$ phase coats the composite-type electrodes in the charging stage, contributing to extending the lifetime of the batteries. K_xMnO_2 electrode with layered birnessite structure shows long cycling life at low current densities (122 mAh g^{-1} at 30 mA g^{-1} after 50 cycles) and good efficiencies (ca. 99%) in the 0.1 Mn^{2+} electrolyte. In contrast, in the 0.5 M Mn^{2+} electrolyte, high values of specific capacity are delivered by the cell at higher rates, that is, 150 mAh g^{-1} at 600 mA g^{-1}. In Mn_5O_8@Mn_3O_4 the good performance is due to the synergistic effect of the two compounds forming the composite. Thus, after more than 100 cycles this composite displays specific capacity values of 175 mAh g^{-1} at 2150 mA g^{-1} in the 0.1 M Mn^{2+}/1 M Zn^{2+} electrolyte.

1. Introduction

It is well-known that MnO_2 exists in various crystal forms such as α-MnO_2, β-MnO_2, ε-MnO_2, γ-MnO_2, δ-MnO_2, and todorokite-type MnO_2. In these structures, the basic structural unit consists of MnO_6 octahedra connected to each other by sharing edges or corners, giving rise to chain, tunnel, and layered structures with enough space to accommodate foreign cations.

Theoretically, MnO_2 could accommodate one inserted Zn^{2+} cation per formula with a high theoretical capacity of approximately 616 mAh g^{-1}, corresponding with the reduction of Mn^{4+} to Mn^{2+} cations. However, in previous literature it has been stated that after the discharge process the Mn ions reach an oxidation state of III, that is, only 0.5 Zn^{2+} ions[1] can actually be inserted per formula-unit in the structure, leading to a maximum theoretical capacity of 308 mAh g^{-1}.

The β-MnO_2 polymorph possesses a rutile-type structure in which tunnels of 2.3×2.3 Å are found. Kim et al.[2] reported that β-MnO_2 delivered a high discharge capacity of 270 mAh g^{-1} at 100 mA g^{-1}, high-rate capability (123 and 86 mAh g^{-1} at 528 and 1056 mA g^{-1}, respectively), and long cycling stability (75% capacity retention with 100% coulombic efficiency at 200 mA g^{-1}) after 200 cycles.[3] That the same year, Zhang[4] demonstrated that on first discharging from β-MnO_2 pirolusite, the rutile structure leads to a layered zinc-buserite, in which zinc cations are allowed to intercalate.

Another important polymorph is the γ-MnO_2 phase, which presents 1×2 (2.3×4.6 Å) and 1×1 tunnels. Mesoporous γ-MnO_2 cathode was reported to deliver a specific capacity of 285 mAh g^{-1} at 0.05 mA cm^{-2}. The mechanisms proposed by Alfaruqi[5] showed that the tunnel-type parent γ-MnO_2 suffers several structural transformations during discharge process. First, the spinel-type Mn(III)-phase ($ZnMn_2O_4$) is obtained. When specific capacity is close to 175 mAh g^{-1}, besides this spinel-phase a tunnel-type γ-Zn_xMnO_2 stabilizes. Finally, at the end of the discharge stage, a layered-type L-Zn_yMnO_2 is also present. All these Mn-multivalent phases coexist after complete electrochemical Zn-insertion, although on successive Zn-deinsertion/extraction most of them revert back to the parent γ-MnO_2 phase.

Perhaps, the most studied polymorph as a cathode in Zn-ion batteries (ZIBs) is α-MnO_2, due to the presence of 1D 2×2 tunnels (4.6×4.6 Å) in its crystal structure, thus allowing fast diffusion for foreign cations along the z-axis as well as efficient storage. Xu et al.[6] reported that the $ZnMn_2O_4$ phase is obtained when Zn^{2+} ions are intercalated through α-MnO_2. Considering

I. Álvarez-Serrano, D. A. Giraldo, M. L. López
Departamento de Química Inorgánica I
Facultad Ciencias Químicas
Universidad Complutense de Madrid
Madrid 28040, Spain
E-mail: marisal@ucm.es

P. Almodóvar
Albufera Energy Storage
Madrid 28049, Spain

F. Llopis, B. Solsona
Departament d'Enginyeria Quimica
ETSE
Universitat de Valencia
Av. Universitat
Burjassot, Valencia 46100, Spain

The ORCID identification number(s) for the author(s) of this article can be found under https://doi.org/10.1002/admi.202101924.

DOI: 10.1002/admi.202101924

 © 2022 Wiley-VCH GmbH

that reversal transformation occurs during the charging process, the authors concluded that the charge-discharge process is highly reversible. Moreover, this result was confirmed by XANES analysis.[7] Besides, Lee et al.[8] showed that a layered structure is formed with an interlayer distance of 11 Å. Therefore, the intercalation of zinc ions into α-MnO_2 leads first to the formation of buserite phase, which evolves through a series of reaction steps to Zn-birnessite phase, which presents an interlayer distance of 7 Å. Concerning the electrochemical response of α-MnO_2, an alternative mechanism implying co-insertion of H^+ and Zn^{2+} has been reported to operate in mildly acidic electrolytes. Moreover, chemical conversion reactions were also considered. In these cases,[9] the cathode experienced a chemical transformation between MnOOH and α-MnO_2.

The δ-MnO_2 layered-type structure can be described in terms of edges-sharing MnO_6 octahedra leading to a layered structure. From it, two forms can be stabilized: one of them is birnessite-type, in which one layer of water molecules in-between the MnO_6 layers exists; and the other is buserite-type structure, in which two layers of water molecules can be found between the octahedra planes.[10] In the battery built by a δ-birnessite-MnO_2 cathode, a capacity fading is unfortunately obtained due to the production of irreversible spinel-type $ZnMn_2O_4$ phase and manganese dissolution.[11] A detailed study[12] in Zn- δ-MnO_2 system revealed a co-insertion mechanism, where Zn^{2+} insertion occurs first, followed by H^+ insertion into the host. In recent literature,[13] it has been reported that $K_{0.8}Mn_8O_{16}$ compound can supply a way of suppressing manganese dissolution via incorporation of K^+ ions, thus intrinsically stabilizing the Mn-based material. Besides, in this kind of birnessite-type phases, simultaneous mechanisms of insertion and conversion reaction based on H^+-storage process can operate, which may contribute to fast kinetics.

Moreover, in addition to manganese (IV) oxides, Mn_5O_8 mixed oxide could be a good candidate as a cathode for ZIBs. All studies reported in the literature indicated that in this compound both Mn(II) and Mn(IV) cations are present, that is, $Mn_2^{2+}Mn_3^{4+}O_8$. Therefore, in principle all manganese ions could be reduced to Mn(II) and up to 3 Zn^{2+} ions could theoretically be inserted, leading to a theoretical specific capacity of 399.5 mAh g^{-1}. Nevertheless, a scenario in which the manganese ions would only be partially reduced to Mn(III) should be taken into account. In this case, Mn(II) and Mn (III) cations would be present in the compound, giving a theoretical capacity of 199.7 mAh g^{-1}. In this sense, the study carried out by Hao et al.[14] showed that Mn_3O_4 undergoes a phase transition to a layered-type birnessite through the formation of Mn_5O_8 as an intermediate product, without the participation of zinc ions at the initial charge process. Although the Mn_5O_8 compound has theoretically lower specific capacity than the MnO_2 oxide, it could constitute an alternative candidate, avoiding the breakdown of the cathode by the dissolution of Mn(III) ions in the slightly acidic electrolytes used in Zn-MnO_2 batteries. Indeed, this oxide could be a more feasible choice as a cathode in Zn ion batteries because of its good performance, and its long cycle life. Moreover, Mn_2O_3-MnO_2 heterostructures have been proposed as a robust cathode for Zn storage.[15]

Therefore, different functional composites can be synthesized from manganese salts (both Mn(II) salts and oxo-composites in which Mn is in a higher oxidation state) with carboxylic acids or with alcohols.[16,17] Interestingly, the obtained products will presumably present different morphologies, which could facilitate the ions' diffusion in the intercalation processes. In this context, we were interested in the study of aqueous zinc-ion batteries with different manganese oxides cathodes. A first charging process up to 2 V will create an interface that could increase the stability of the battery. Under this approach, this article analyses the electrode-electrolyte interface and identifies the species that are deposited on the surface. The role of such species is related to the electrochemical behavior displayed by the material and the cyclability of the batteries is studied both at low and high current densities after many cycles.

2. Results and Discussions

2.1. Synthesis of Materials

Two methods have been employed in the synthesis of manganese oxides to be used as cathodes in zinc batteries. On the one hand, the manganese composites were synthetized from Mn(II) salts and organic acids.[16] In a typical synthesis, 3 g of $Mn(NO_3)_2$ and 19.5 mL of 20% glyoxylic acid or 21 mL of ketoglutaric acid 3 M were mixed. This mixture was left on a hot plate stirrer heating under constant stirring until a gel was formed. Each sample was calcined in flowing air according to the following sequence: 55 °C/1 h ramp/120 °C/1 h hold/1h ramp/350 °C/4 h hold. These samples hereinafter are called MnG and MnK, respectively.

On the other hand, the manganese oxides with birnessite structure were prepared from 20 mL of $KMnO_4$ 0.3 M using ethylene glycol as the reductor. In this way, a solution of ethylene glycol was added drop by drop until a change of color of the $KMnO_4$ solution was observed, and then 8 mL of water was added. This mixture was left on a hot plate stirrer heating under constant stirring until a gel was formed. Subsequently, the sample was filtered and dried in a stove at 80 °C for 12 h. Following a thermal treatment of 400 °C for 4 h. was carried out.[17] This sample is hereinafter referred to as KMn.

2.2. Structural and Microstructural Characterization

Figure 1a shows the X-ray diffraction patterns for the MnG and MnK samples together with the corresponding diffractograms of Mn_3O_4 (PDF 24–734), Mn_5O_8 (PDF 1-72-1427), and Mn_2O_3 (PDF 41–1442).

Most of the diffraction maxima of the MnG diagram belong to Mn_3O_4 structure, whereas maxima appearing at 2θ values of 21.6° and 47.8° could be only assigned to Mn_5O_8. In order to confirm the occurrence of both structural phases, a Rietveld refinement was performed in which the structural data of both phases were included. The good fit achieved between the experimental and theoretical profiles is presented in Figure S1, Supporting Information, and the R-factors as well as the most relevant crystallographic data are included in Table S1, Supporting Information. From these results, it can be stated that both phases in a ≈1:1 ratio are simultaneously stabilized in the

© 2022 Wiley-VCH GmbH

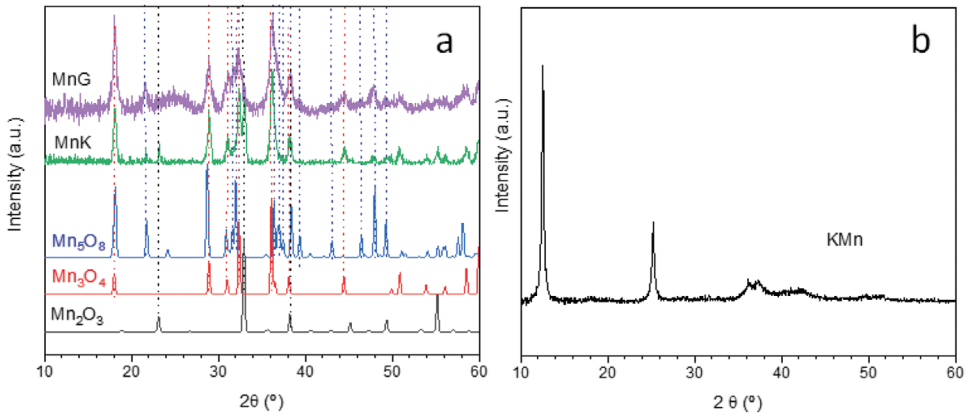

Figure 1. X-ray diffraction patterns of a) MnG and MnK, together with theoretical profiles of Mn_3O_4 (PDF 24–734), Mn_5O_8 (PDF 1-72-1427), and Mn_2O_3 (PDF 41–1442), and b) KMn.

sample via calcination. Consequently, a well-defined Mn_3O_4@ Mn_5O_8 heterostructure is obtained at 350 °C.

The XRD pattern of MnK also shows characteristic Mn_3O_4 peaks as well as several maxima of very low-intensity corresponding to Mn_5O_8. In this case, two new peaks appearing at 2θ values of 23.2° and 33.1° can be clearly assigned to the Mn_2O_3 phase. Accordingly, the MnK sample is mostly composed of Mn_3O_4 and Mn_2O_3 and a small quantity of Mn_5O_8 may also be found.

Finally, the XRD pattern of KMn, Figure 1b, exhibits basal reflections at 2θ values of 12.5° and 25.3°, being these features typical of the lamellar birnessite structure. In this sample there is a high degree of disorder as evidenced in the diffractogram by the appearance of two broad bands around 37° and 42° 2θ values. These results are in good agreement with previously published works.[18,19]

EDX analysis for the KMn derivative indicates the presence of K (Figure S2, Supporting Information), and examination of a representative number of crystals leads to a mean composition of $K_{0.3}MnO_2$, characteristic of birnessite structure.[20] In addition, the thermogravimetric analysis (TGA) in the temperature range from 50 to 600 °C (Figure S3, Supporting Information) displays three regions where the decomposition takes place. The initial weight loss up to 150 °C can be associated to the evaporation of the surface-adsorbed water (ca. 3%), whereas the second region up to 250 °C can be attributed to the dehydration of interlayer water (ca. 6.5%). Then, the formula for this material can be written as $K_{0.3}MnO_2$ $0.4H_2O$. Finally, the weight loss of 2.5%, obtained when the material is heated above 250 °C, is usually associated with oxygen loss.[21] Furthermore, when the material is heated up to 600 °C, it does not transform into a 2×2 channel structure as previously suggested,[22] as indicated by the XRD diagram of the residue.

The morphology of the samples was explored by scanning electron microscopy (SEM) and high-resolution transmission electron microscopy (HRTEM), and **Figure 2** shows representative images obtained for each sample. The MnG sample presents a rod-like morphology, with width ranging from 0.6 up to 1.2 µm (Figure 2a). A different conformation is observed for MnK sample, in which two types of morphologies can be appreciated: "'cloud-like"' particles, and partially fused particles with flake-like morphology. Finally, in Figure 2d the fibrous morphology of KMn sample with lattice fringes reflecting the (001) lattice planes is evidenced. Figure S4, Supporting Information, shows a more detailed microstructural characterization for this sample.

2.3. Electrochemical Characterization

2.3.1. Cathodic Reactions

The electrochemical tests started with the charging process at voltages up to 2V. **Figure 3**a,b shows the corresponding curves for MnK and MnG with three different electrolytes: 0.5 M $MnSO_4$ and 0.5 M $ZnSO_4$, 0.1 M $MnSO_4$ and 1 M $ZnSO_4$, and 2 M $ZnSO_4$, denoted as 05Mn05Zn, 01Mn1Zn, and 2Zn, respectively. In these charge profiles, only a plateau at 1.98 V appears, and the value of specific capacity obtained is strongly dependent on the electrolyte employed. The highest capacity values were achieved for MnK and MnG electrodes when the 05Mn05Zn electrolyte was utilized, 1374 and 801 mAh g^{-1}, respectively. These profiles present similar features to those encountered in deposited MnO_2 cathodes obtained by Li.[23]

Nonetheless, with the 01Mn1Zn electrolyte the specific capacity is only 131 mAh g^{-1}. The XRD pattern of MnK electrode charged up to 2V (Figure S5, Supporting Information) presents practically the same peaks as those observed in the original diffraction profiles. Two extra small maxima can be appreciated, identified as $ZnSO_4$ $6H_2O$ (PDF 1–352), probably due to a slight contamination of $ZnSO_4$ from the electrolyte. On the second discharge process down to 0.8 V two plateaus at average voltage values of 1.4 and 1.3 V are clearly seen. The first slope line at 1.4 V can be ascribed to the H^+ insertion whereas the flat plateau at 1.3 V is due to the insertion of Zn^{2+} cations[24] (Figure S6, Supporting Information). In the XRD diagram corresponding to the discharged electrode (Figure S5, Supporting Information), the peaks located at 20.2° and 21.9° (2θ) (previously indexed to $ZnSO_4$ $6H_2O$) disappear. However, a new maximum at 8.5° (2θ) appears, which could be assigned to $Zn_4(SO_4)(OH)_6$ $4H_2O$ (PDF-044-0673) phase. As previously suggested,[23–25] in addition to this phase, the MnOOH phase

© 2022 Wiley-VCH GmbH

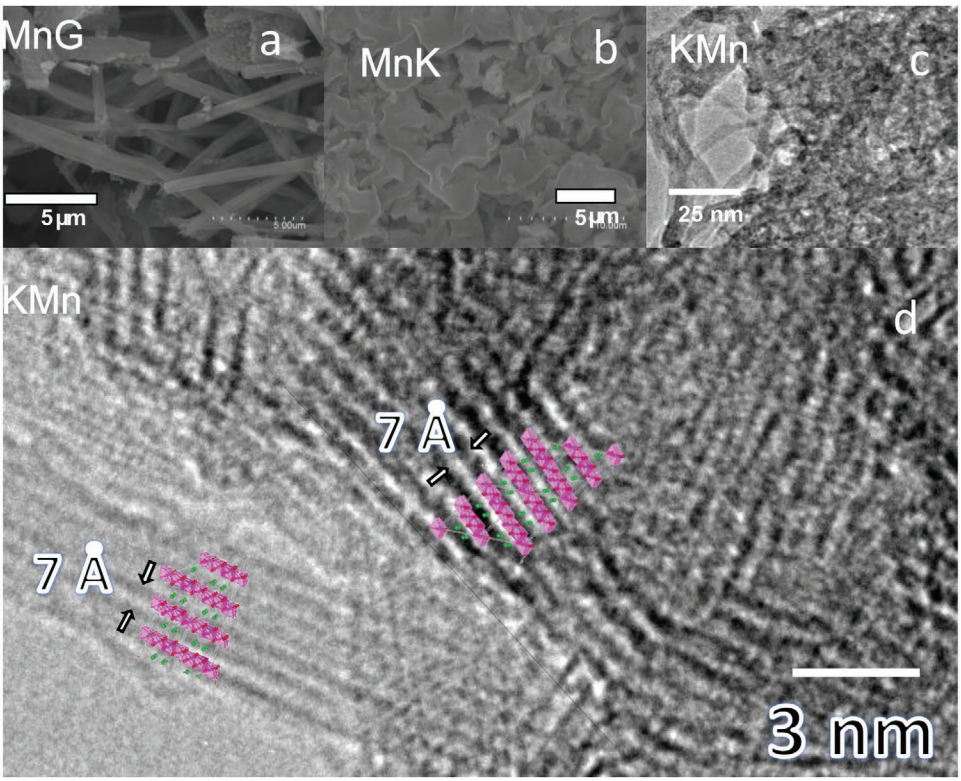

Figure 2. SEM images of a) MnG and b) MnK; and HRTEM images for c) KMn and d) KMn (MnO_6 polyhedra and K ions positions of the birnessite structure are superimposed for clarity).

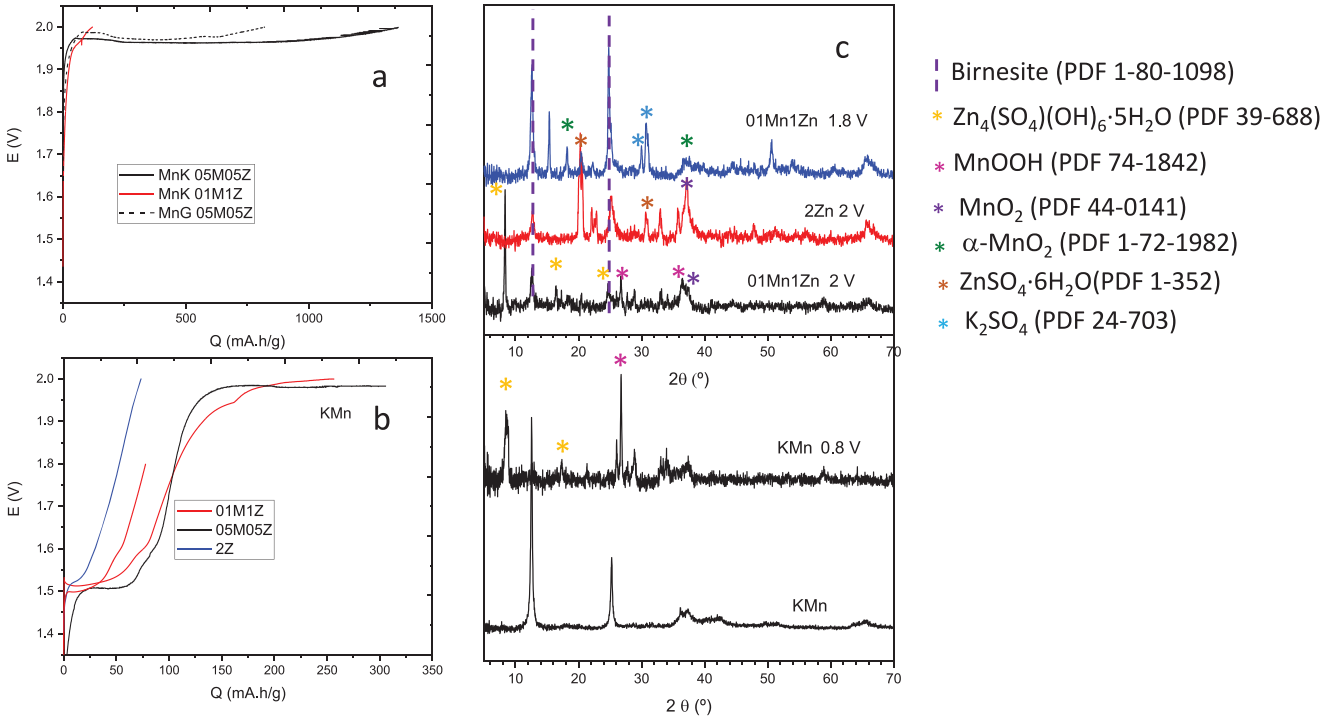

Figure 3. a) Charge tests for MnK and MnG up to 2V in different electrolyte media. b) Charge tests for KMn up to 2 and 1.8 V in different electrolyte media. c) Ex situ XRD profile of KMn in different electrolytes after charging up to 1.8 or 2V and discharging down to 0.8 V.

© 2022 Wiley-VCH GmbH

and other manganese oxides (Zn_xMnO_2, $ZnMn_3O_7$, Mn_3O_4....) would probably stabilize. However, they could be hardly detected, as their most intense peaks appear at 2θ-values very close to those corresponding to the original electrode.

Compared with MnK and MnG electrode, the charge profiles of KMn cathode in different electrolytes and up to 2 V reveal smaller specific capacity values (Figure 3b). Moreover, together with the previously observed plateau at 1.98 V, a second plateau at 1.55 V is now appreciated. However, in the 2Zn electrolyte, only a plateau at lower voltage is seen. The ex situ XRD pattern corresponding to the charging process (Figure 3c) reveals that the peaks' positions of the oxides remain unchanged, although several changes in intensity are observed. In addition, in the XRD profile of KMn cathode charged up to 2V in 01Mn1Zn new maxima appear, which could be indexed to $Zn_4(SO_4)(OH)_6$ $3H_2O$ (PDF-039-0688), MnOOH (PDF 74–1842), and MnO_2 (PDF-44-0141). The MnO_2 phase is also observed in XRD profile corresponding to KMn cathode charged up to 2 V in 2Zn electrolyte. It is worthwhile noting that these compounds are clearly seen at the charging process, contrary to that reported in previous works,[23,26] in which these phases were only stabilized in the discharge regime.

Therefore, it can be assumed that the presence of Mn^{2+} in the electrolyte plays a key factor. Having in mind these considerations, the reactions that could be taking place in the charging process of the KMn cathode could be summarized as follows:

$$Mn^{2+} + 1/4O_2 + 7/2H_2O \rightarrow MnOOH + 2H_3O^+ \quad (1)$$

$$Mn^{2+} + 1/2O_2 + 3H_2O \rightarrow MnO_2 + 2H_3O^+ \quad (2)$$

$$\text{Electrolyte: } Zn(H_2O)_x^{(2+)} \rightarrow [Zn(H_2O)_x(OH)]^+ + H_3O^+ \quad (3)$$

$$[Zn(H_2O)_x(OH)]^+ + 1/4SO_4^{2-} \rightarrow Zn(SO_4)_{1/4}(OH)_{3/2}\cdot xH_2O \quad (4)$$

As carried out for the MnK electrode, the KMn composite was cycled two times (Figure S6, Supporting Information). Again, on the discharge down to 0.8 V, two plateaus are appreciated at average voltages of 1.4 and 1.3 V, which can be attributed to the H^+ insertion and to H^+/ Zn^{2+} conversion reactions, respectively.[24] Only slight differences could be observed in the XRD diagram when compared to the profile of the charged sample (Figure 3c). The peak close to 8.5° (2θ) appears broader, suggesting that the $Zn_4(SO_4)(OH)_6.xH_2O$ (ZHS) phase is stabilized with different hydration degrees (PDF-39-688; 39–689; 39–670; 44–673). Besides, the maxima corresponding to MnOOH have now grown up in intensity. Therefore, the following reactions could be representative of the electrochemical process taking place in the KMn electrode:[26]

$$\text{Cathode: } MnO_2 + H_3O^+ + 1e^- \rightleftharpoons MnOOH + H_2O \quad (5)$$

$$\text{Anode: } 1/2Zn \rightleftharpoons 1/2Zn^{2+} + 1e^- \quad (6)$$

$$\text{Electrolyte: } Zn(H_2O)_x^{(2+)} \rightarrow [Zn(H_2O)_x(OH)]^+ + H_3O^+ \quad (7)$$

Overall reaction:

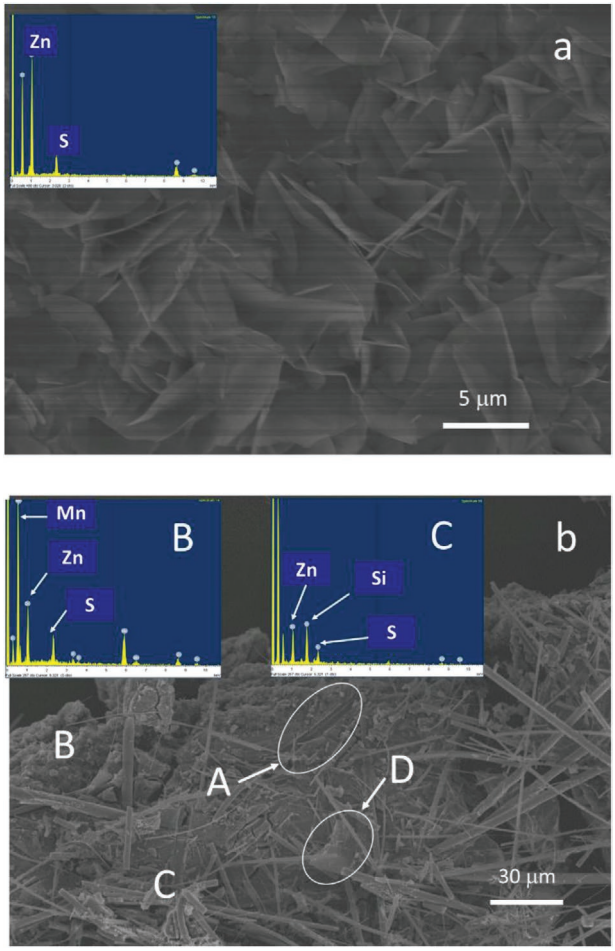

Figure 4. SEM images of KMn in 01Mn1Zn electrolyte after a) discharging down to 0.8 V (inset includes the EDX spectrum), and b) charging up to 2 V. A, B, C, and D refer to regions in which different morphologies are appreciated. Insets show EDX corresponding to B and C regions.

$$MnO_2 + 1/2Zn + 1/6ZnSO_4 + (x/6+1)H_2O \rightleftharpoons 1/6Zn(SO_4)[Zn(OH)_2]_3\,xH_2O + MnOOH \quad (8)$$

Figure 4a gathers a micrograph of the KMn electrode after the discharge, showing large flake-like formations typical of ZHS.[27] Indeed, the EDX analyses (inset of Figure 4a) reveal the presence of both Zn and S. On the other hand, Figure 4b shows a representative SEM image of KMn electrode after the charging process. Four morphologies can be observed in different regions, marked as A, B, C, and D in the image. In A, embedded sheets of ZHS are seen, coherently with the EDX analyses (not shown). In B nanoparticles are observed. The corresponding EDX analysis (inset of Figure 4b) is concordant with the presence of a new compound containing K-Zn-Mn, coherently with the changes observed in the XRD pattern of the charged sample. In C, a morphology with rod-like appearance can be appreciated, similar to that observed in the starting KMn material. The silicon detected in the corresponding EDX spectrum (inset of Figure 4b) could be ascribed to the whatman separator used in the electrochemical cell. Finally, in D a morphology consisting of fine sheets of ZHS phase is observed.

© 2022 Wiley-VCH GmbH

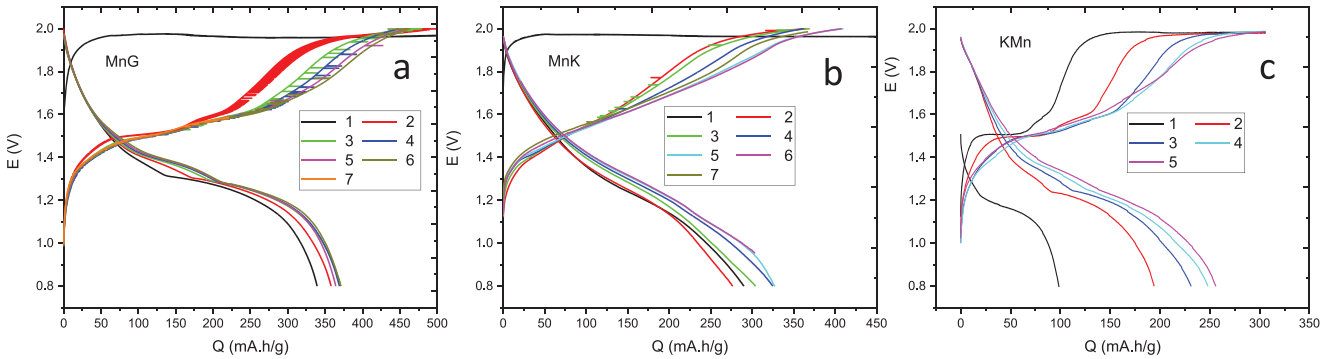

Figure 5. Charge-discharge profiles at 60 mA g^{-1} in 05Mn05Zn electrolyte for a) MnG, b) MnK, and c) KMn.

Indeed, the EDX analyses carried out on these sheets revealed the presence of only Zn and S, suggesting that ZHS is also formed in the charging stage.

As it is well known, the electrochemical deposition of MnO_2 from Mn(II) in this mild aqueous electrolyte occurs at the potentials more positive than those needed for the oxidation of Mn (III) to MnO_2. At this high potential range, oxygen evolution is inevitable.[28] In order to study the upper voltage limits, charge test up to 1.8 V in the 01Mn1Zn and 2Zn electrolyte (Figure 3b) and the respective ex situ XRD pattern of the cathode after being charged (Figure 3c, blue line and Figure S7, Supporting Information) were made. When Mn^{2+} is absent in the electrolyte, the XRD profile of the charged cathode until 2 V does not show any evidence of new peaks. However, some changes are seen in the 01Mn1Zn electrolyte. It is worth noting that the maximum at a low angle (8.5°) typical of the ZHS phase is absent. Besides, peaks of $ZnSO_4$ (JCPDS 1–352) can be now observed. Further, a peak around $2\theta = 30°$ was assigned to K_2SO_4. Thus, the presence of these phases on the electrode surface seems to confirm the partial solution of the sample ($K_{0.3}MnO_2$), that is, K^+ and Mn^{3+} ions which were located above or below edge-sharing $Mn^{4+}O_6$ octahedra sheets are now in dissolution. Moreover, the maxima corresponding to α-MnO_2 (JCPDS 1-72-1982) are identified in the XRD profile. On the other hand, the characteristic peaks of the birnessite phase appearing around 12 and 25° (2θ), exhibit anomalous intensities, that is, ≈I(12°)–I (25°). A plausible explanation for this fact could be related to $Mn^{4+}O_6$ octahedra interlayer occupation, as evidenced by theoretical profiles calculated from different occupations in these interlayer spaces, where Zn^{2+} ions and water molecules could be located (Figure S8, Supporting Information). Therefore, considering that both compounds could be present after the charging process, the following reactions could be suggested:

$$Mn^{2+} + 1/2O_2 + 3H_2O \rightarrow MnO_2 + 2H_3O^+ \quad (9)$$

$$Mn^{2+} + xZn^{2+} + 3H_2O + 1/2O_2 \rightarrow Zn_xMnO_2 + 2H_3O^+ \quad (10)$$

2.3.2. GDC Study: 05Mn05Zn

Figure 5 shows charge-discharge profiles of the three prepared samples at 60 mA g^{-1}, between 2 and 0.8 V, employing the 05Mn05Zn electrolyte. It can be observed how from second charge profiles onwards, the plateau at 2V decreases whereas the plateaus at 1.5 and 1.6 V increase as cycle number increases. The observed behavior of the different charge-discharge profiles of the three samples, MnK, MnG, and KMn is similar to that reported previously in literature for Zn-manganese oxide batteries.[29]

Figure 6 gathers the efficiency and specific capacity values for all samples at different rates. Moreover, **Table 1** depicts the most relevant values. It can be observed that at low current density values (60 mA g^{-1}), both the MnG and MnK samples achieve capacity values higher than the theoretical one (considering 0.5 Zn^{2+} inserted ions per formula), even at the fifth cycle. Conversely, KMn sample only achieves a capacity value of 256 mAh g^{-1}, (below the theoretical one). The better cyclability of both MnG and KMn could be due to their rod-type microstructure. Specifically, MnG electrode delivers the highest

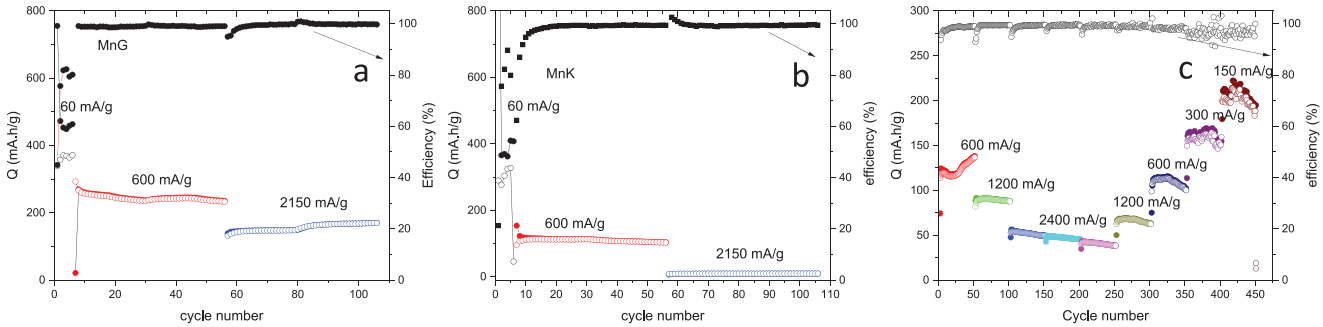

Figure 6. Specific capacity and efficiency at different current densities for electrodes a) MnG, b) MnK, and c) KMn in the 05Mn05Zn electrolyte.

© 2022 Wiley-VCH GmbH

Table 1. Specific capacity values (mAh g^{-1}) in charge (Q_c) and discharge (Q_d) processes for MnG, MnK, and KMn at different applied current densities and in different cycles. The cycle number is indicated in brackets.

Rate	60 mA g^{-1}		600 mA g^{-1}		1200 mA g^{-1}		2200 mA g^{-1}	
	Q_c	Q_d	Q_c	Q_d	Q_c	Q_d	Q_c	Q_d
MnG	463 (6)	371 (6)	235 (56)	233 (56)			168 (100)	168 (100)
MnK	410 (6)	327 (6)	104 (56)	103 (56)			10 (100)	10 (100)
KMn	256 (6)	236 (6)	136 (50)	138 (50)	88 (100)	87 (100)	49 (100)	49 (100)

specific capacity values at any current rate. This superior electrochemical property could be probably related to the existence of Mn_5O_8, and the easy transformation of this compound to the birnessite structure. Finally, it is worth mentioning that the MnK cathode at high current density shows a sharp fall of the capacity probably triggered by the loss in crystallinity of the cathode material, that is, corresponding XRD pattern (not shown) is coherent with a clear amorphous character.

However, in the case of the MnG cathode, some peaks of low intensity were still observed after long-time cycling (**Figure 7**). Even although XRD data are not unambiguous due to low crystallinity of the obtained products, some features could be pointed out:

The most intense maximum observed in the XRD pattern of the material after the 36th discharge cycle (Figure 7) could be indexed to a δ-MnO_2 phase (PDF 18–802) presenting preferred orientation.[30] Actually, these XRD profiles could be also indexed to a mixture of $ZnMn_3O_7$ (PDF 30–1483) and spinel phase $ZnMn_2O_4$ (PDF 24–1133). The same phases were observed in the XRD pattern after the 500th discharge cycle, where additional maxima appearing could be indexed as $ZnSO_4.6H_2O$ (1–352), thus confirming that these phases form as the charge-discharge galvanostatic process goes on. Indeed, after successive cycling of the Mn_3O_4@Mn_5O_8 electrode, Zn^{2+} ions become intercalated between MnO_6-octahedra sheets giving rise to $ZnMn_3O_7$ compound. Moreover, a $ZnMn_2O_4$ phase is also stabilized, which is probably responsible for the observed capacity loss.

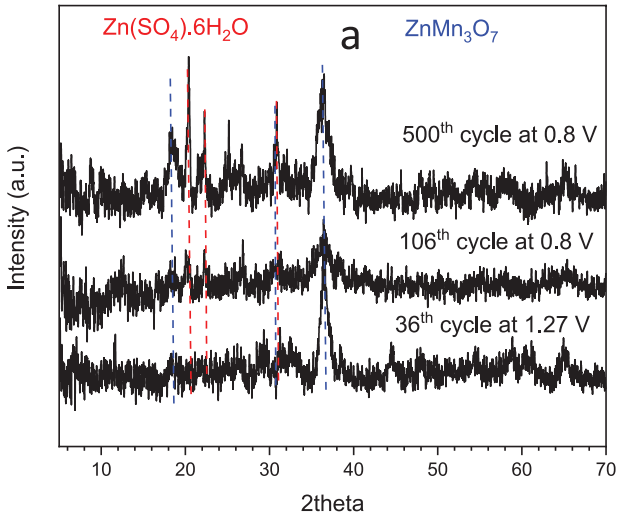

Figure 7. MnG cathode XRD pattern after the charge-discharge test.

2.3.3. GDC Study: 01Mn1Zn

Figure 8 shows the cycling performance of the batteries constructed with the studied electrodes using 01Mn1Zn as electrolyte. The MnG cathode delivers a capacity of 164 mAh g^{-1} and a capacity retention of 45% after cycled 500 times at 600 mA g^{-1} (Figure 8a). In contrast, the MnK cathode shows an initial capacity of just 78 mAh g^{-1} at a current rate of 166 mA g^{-1}, but after 49 cycles it delivers capacity values of around 245 mAh g^{-1}. The enhancement of capacity can be interpreted considering cathode wettability, gradual activation of the cathode, and structural changes of the sample.[31] In addition, a gradual activation of the cathode results from the reoxidation of Mn^{2+} in the electrolyte into new active MnO_2, as previously suggested.[32] Nevertheless, the capacity drops drastically at 108 mAh g^{-1} after 130 cycles, corresponding to a retention of 44%.

An activation of the cathode at low rates is also observed for KMn (Figure 8c). The KMn cell delivers a capacity of 336 mAh g^{-1} at 60 mA g^{-1} current rate. When the current density is increased up to 600 mA g^{-1} the capacity is reduced to 190 mAh g^{-1}. Furthermore, when the cathode is cycled 300 times the capacity value only decreases to 114 mAh g^{-1}.

Therefore, all batteries are activated at low rates and they show a good electrochemical response at a current density of 600 mA g^{-1}. Among the studied cathodes, MnG presents the best performance whereas MnK is not actually an adequate candidate for a competitive Zn battery.

To better understand the influence of material activation on the cycling performance, galvanostatic charge and discharge (GCD) tests for KMn were carried out at higher rates, 300 and 1600 mA g^{-1} (**Figure 9**a,b). As it can be appreciated, both the specific capacity and cycle performance of this cathode are practically independent of the activation process. Besides, the capacity retentions are significantly better at higher discharge/charge rates, in good agreement with the literature.[24]

Finally, complementary rate performance measurements were performed by increasing the current density from 30 to 240 mA g^{-1} every 50 cycles (Figure 9c). Although the obtained capacity values at different rates are only moderate, they are again achieved when returning to the given current density. Thus, at 120 mA g^{-1}, the discharge capacity values after 150, 250, and 400 cycles are 60, 62, and 71 mAh g^{-1}, respectively. Also, comparing the values at 30 mA g^{-1}, the same value of 122 mAh g^{-1} is reached after 50 and 370 cycles, demonstrating excellent rate capability. Hence, this KMn cathode shows a very good performance even after 500 discharge-charge cycles.

Complementary, aiming to study the influence of the MnO_2 interface obtained at 2 V in electrolytes without Mn^{2+}, the KMn electrode in 2Zn electrolyte was tested in the voltage window

© 2022 Wiley-VCH GmbH

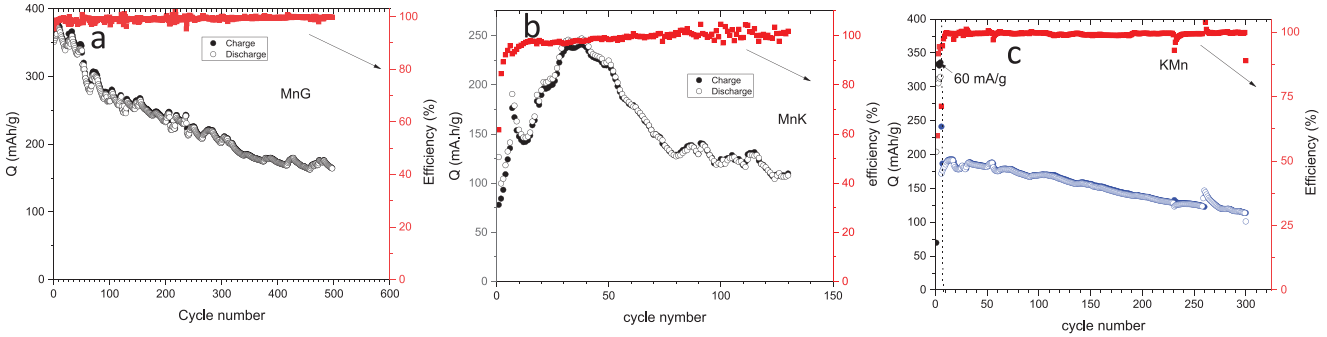

Figure 8. Cycling performance of a) MnG at 600 mA g^{-1}, b) MnK at 166 mA g^{-1}, and c) KMn five cycles at 60 mA g^{-1} and then the current density is increased up to 600 mA g^{-1}, in the 01Mn1Zn electrolyte.

1.8–0.8 V. First, no significant differences in the XRD profile of the KMn cathode before (Figure S7, Supporting Information, black line) and after (Figure S8, Supporting Information, red line) the charging up to 1.8 V are evidenced, indicating that no changes are generated in the cathode interphase. Second, the cathode was checked at 30 and 300 mA g^{-1} rates, delivering low values of capacity, 134 and 60 mAh g^{-1}, respectively. Thus, the capacity losses after 50 cycles are of 35% at 30 mA g^{-1} and of 55% at 300 mA g^{-1} (**Figure 10**). However, taking into account the data presented in Figure 8c, the capacity loss after 100 cycles at 600 mA g^{-1} for KMn is 11%, in the electrolyte 01Mn1Zn (data calculated from the capacity of the fifth cycle). Therefore, the phases formed when the electrodes are subjected to 2 V in aqueous solutions of $MnSO_4$ and $ZnSO_4$ provoke an interphase activation leading to enhancement of electrochemical response.

2.3.4. CV Analyses

Figure 11 shows cyclic voltammetry (CV) curves for assembled ZIBs using different current rates and two different electrolytes for MnG and KMn. Their general aspect is similar to that previously found in other Mn-oxide ZIBs.[14,33,34] From the second cycle, two reduction peaks appear at 1.30 and 1.20 V. Besides, an oxidation peak at 1.55 V and a small shoulder at 1.65 V are also observed. The voltage values of each peak are dependent on the scan rate. Thus, as this rate increases, the reduction peaks slightly move towards smaller voltage values whereas the oxidation peaks shift to higher values. This gradual voltage change can be attributed to the ion diffusion.[35] At the discharge processes, as the CV rate increases the high-voltage peak remains present and even more intense (due to H^+ insertion), while the low-voltage peak gradually decays (related to Zn^{2+} reaction).

The capacitive and diffusive contributions have been obtained following the procedure described in the Supporting Information file, and they are shown in **Figure 12**. The diffusive percentage obtained for each sweep rate is also gathered in Table S2, Supporting Information. As expected, the ion-diffusion contribution decreases to very low values as the scan rate increases, for example, 17% at 1 mV s^{-1} for MnG in the 05Mn05Zn electrolyte. The MnG/05Mn05Zn, MnG/01Mn1Zn, and KMn/05Mn05Zn batteries, tested up to 2 V show at most scan values a capacitive contribution near 40%. In contrast, a diffusion-controlled intercalation process is the main contribution to the overall kinetic process of the battery KMn/01Mn1Zn, which was cycled until 1.8 V. The capacitive or diffusive behavior found for the different electrodes could be interpreted in terms of their specific capacity values. Thus, the higher capacity values displayed by MnG at any current density and its good cycling performance at high rates can be related to its great capacitive character. In contrast, the KMn electrode shows smaller specific capacity values but the capacity retention seems to be better. Besides, this cathode presents a good capacity retention at low current densities, probably due to its higher diffusive contribution.

Finally, aiming to find out how the cycles number can modify the reactions voltage values, in Figure S10, Supporting

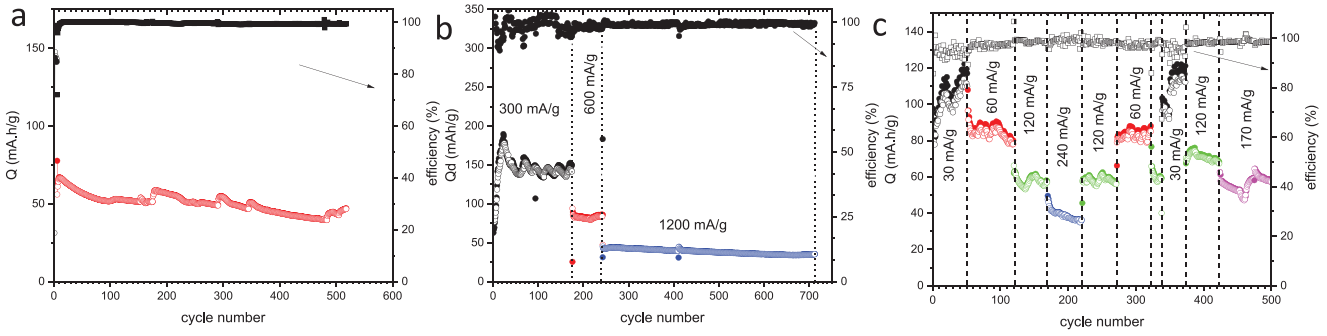

Figure 9. Rate performance of KMn in the 01Mn1Zn electrolyte with activation cycle number of a) 5 cycles at 300 mA g^{-1} and then the current density was increased to 1600 mA g^{-1}; b) 175 cycles at 300 mA g^{-1}, 50 cycles at 600 mA g^{-1} and then the current density was increased to 1200 mA g^{-1}. c) Rate performance at different current rates.

© 2022 Wiley-VCH GmbH

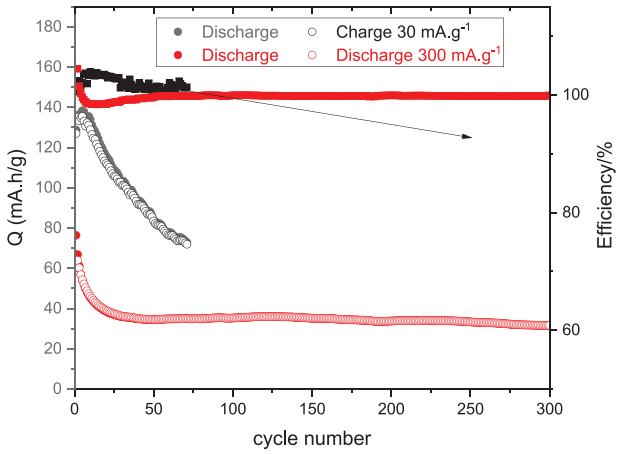

Figure 10. Discharge and charge capacity values and efficiency versus cycle number for KMn at 30 and 300 mA g^{-1} rates.

Information, the voltagrams after several cycles at different current densities are depicted. Broad redox peaks in CV data can be observed, which indicate a pseudocapacitive behavior. Moreover, ΔE (calculated as E_{anodic}–$E_{cathodic}$) is small or remains constant over a wide range of sweep rates.

3. Conclusions

Mixed-valent manganese oxides with different morphologies are obtained using simple syntheses and cheap reagents. On the one hand, the oxidation of a Mn(II) salt with carboxylic acids and subsequent thermal treatment leads to two types of composites with different grain morphology: Mn_2O_3@Mn_3O_4 composites with a plate like morphology, and Mn_5O_8@Mn_3O_4 with rod shape. On the other hand, the oxidation of $KMnO_4$ with ethylene glycol followed by the appropriate heating treatment, produces a birnessite-type manganese oxide with a rod-shaped microstructure.

Charging tests up to 2 and 1.8V in different electrolytes containing different Mn^{2+} concentrations are carried out, thus highlighting the role of Mn^{2+} cations in the Zn battery. For all the cathodes, the plateau appearing at 2V is dependent on the electrolyte employed and is only noticeable when Mn(II) cations are present in the electrolyte medium. In this situation, the appearance of ZHS phases with different hydration degrees in the charging process is appreciated, contrary to previously reported results which establish that these modifications take place at the discharging state. A particular situation is found during operation of the batteries with the KMn cathode, where a new plateau at 1.5 V appears: different species are formed, which are dependent both on the concentration of Mn^{2+} cations in the electrolyte and the voltage. Several manganese phases have been identified that probably contribute to the good performance, long battery life, and cyclability. In addition, a mainly diffusive mechanism operates even at high rates, in good agreement with the nature of the different Mn species formed after the charging process.

Nevertheless, the MnG electrode, consisting of Mn_5O_8@Mn_3O_4 composite delivers a specific capacity of 170 mAh g^{-1} after 105 cycles, at current densities of 2150 mA g^{-1}

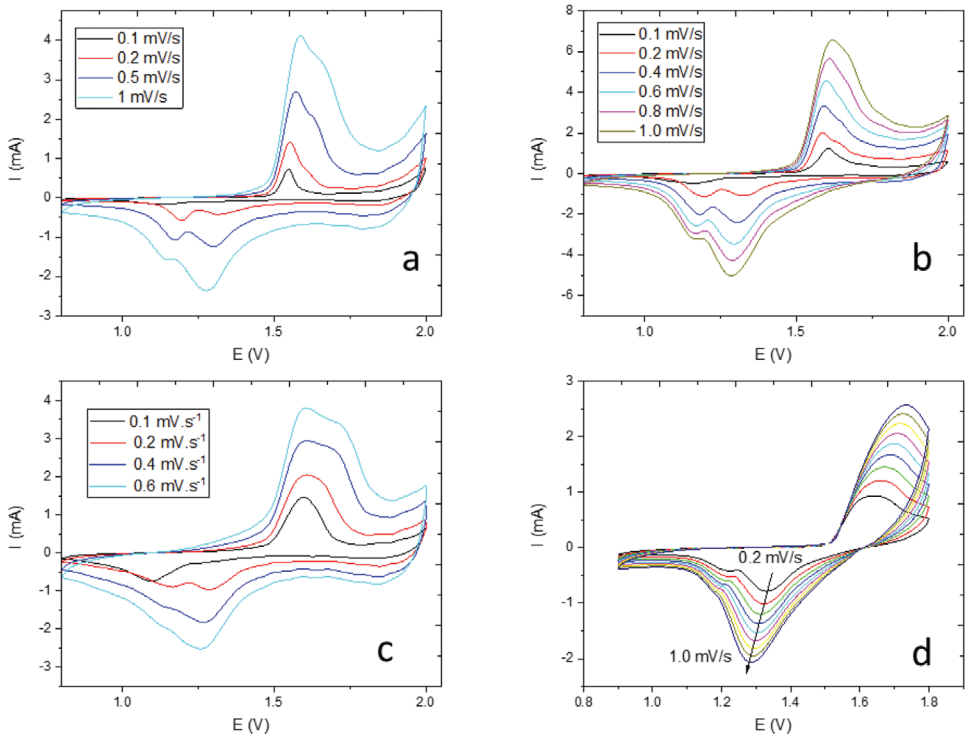

Figure 11. CV curves for a) MnG in 05Mn05Z electrolyte; b) MnG in 01Mn1Zn electrolyte; c) KMn in 05Mn05Zn electrolyte; and d) KMn in 01Mn1Zn electrolyte.

© 2022 Wiley-VCH GmbH

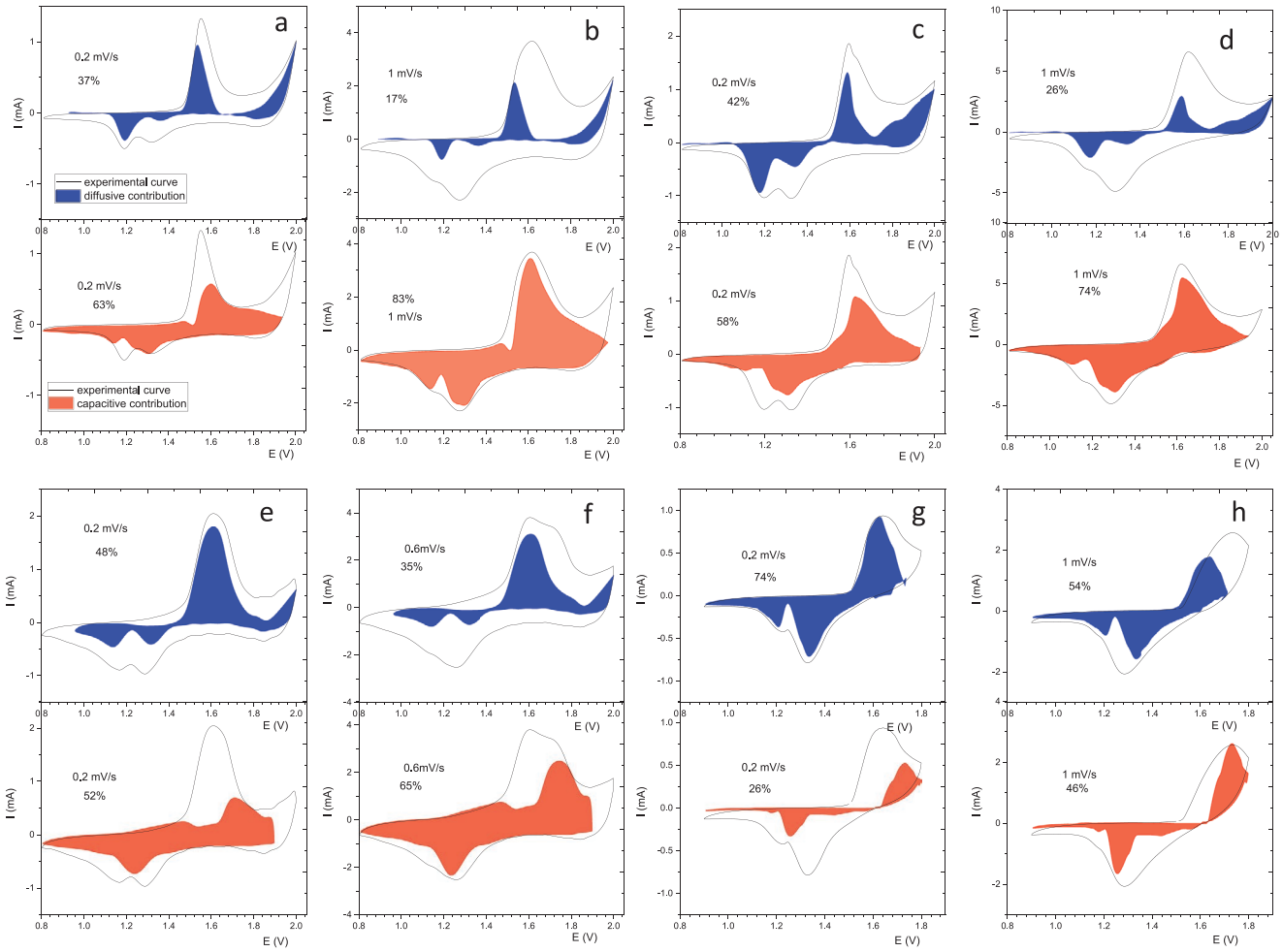

Figure 12. Capacitive and diffusion-controlled contribution analysis of the CV curves of MnG in 05Mn05Z a) at 0.2 mV s^{-1} and b) 1mV s^{-1}; MnG in 01Mn1Zn c) at 0.2 mV s^{-1} and d) 1mV s^{-1}; KMn in 05Mn05Z e) at 0.2 mV s^{-1} and f) 0.6 mV s^{-1}; KMn in M10Z g) at 0.2 mV s^{-1} and h) 1mV s^{-1}.

in the 05Mn05Zn electrolyte. Even at 600 mA g^{-1} this electrode gives specific capacity values of 175 mAh g^{-1} after 500 cycles in 01Mn1Zn electrolyte. Moreover, these high capacitance values are in good agreement with the fact that capacitive behavior is mainly involved.

Finally, it is interesting to highlight that the different species formed when the electrodes are subjected to 2 V in aqueous solutions of $MnSO_4$ and $ZnSO_4$ provoke an interphase activation, leading to an enhancement of the electrochemical response.

4. Experimental Section

Material Characterization: X-ray powder diffraction (XRD) patterns were registered at room temperature with a PANanalytical X'PERT POWDER diffractometer using Cu (Kα) radiation with $\lambda = 1.5406$ Å. Data were collected in the range $5° \leq 2\theta \leq 120°$ range with a step of 0.0167° and analyzed by the Rietveld profile method[36] using the WinPLOTR/Fullprof suite program.[37]

HRTEM was performed in a JEOL 300FEG. The composition of the obtained materials was established by semi-quantitative chemical analysis using energy-dispersive X-ray spectroscopy (EDXS). The samples were prepared by crushing the powders under n-butanol and dispersing it over copper grids covered with a holey carbon film. SEM images and corresponding EDXS spectra were obtained with a JEOL JSM 6335F microscope. Samples were mounted on SEM stubs using carbon adhesive and sputter-coated gold. TGA was carried out under nitrogen by a Pyris thermogravimeter (PerkinElmer, Waltham, MA, USA). The analyses were carried out at a heating/cooling rate of 10 °C min^{-1}.

Electrochemical Characterization: The electrochemical tests of half cells were performed in Swagelok-type cells assembled in an argon-filled dry box, using graphite paper as current collector (for both anode and cathode electrodes), Zn disk as the anode, and Whatman GF/D borosilicate glass fiber sheets and solutions of $ZnSO_4$ $7H_2O$ and $MnSO_4$ H_2O (Sigma-Aldrich) of various concentrations as electrolyte. Three electrolytes were used: 0.5 M $MnSO_4$ and 0.5 M $ZnSO_4$, 0.1 M $MnSO_4$ and 1 M $ZnSO_4$, and 2 M $ZnSO_4$. The synthesized samples were mixed with carbon SP and sodium alginate in deionized water with mass proportions 70:20:10, respectively. The resultant slurry was coated onto the graphite paper and dried at air overnight. The resulting electrodes had an active material loading of about 1–3 mg.

Electrochemical Measurements: Electrochemical testing was done using a Biologic 815 potentiostat. CV and GCD tests were conducted in a potential window between 0.8 and 2.0 V. Different scan rates were applied for CV testing, as well as several different applied specific currents were used for GCD testing. The applied current densities were normalized to the mass of manganese oxide on the electrode.

© 2022 Wiley-VCH GmbH

Supporting Information

Supporting Information is available from the Wiley Online Library or from the author.

Acknowledgements

Authors are grateful to the CAI centers of UCM (XRD and electron microscopy). This work has been supported by MINECO through projects MAT2017-84118-C2-2-R and MAT2017-84118-C2-1-R.

Conflict of Interest

The authors declare no conflict of interest.

Data Availability Statement

Data available in article supplementary material.

Keywords

birnessites, manganese oxides, zinc-ion batteries

Received: October 6, 2021
Published online:

[1] Y. Zhao, Y. Zhu, X. Zhang, *InfoMat* **2020**, *2*, 237.
[2] S. Kim, K. W. Nam, S. Lee, W. Cho, J.-S. Kim, B. G. Kim, Y. Oshima, J.-S. Kim, S.-G. Doo, H. Chang, D. Aurbach, J. W. Choi, *Angew. Chem., Int. Ed. Engl.* **2015**, *54*, 15094.
[3] S. Islam, M. H. Alfaruqi, V. Mathew, J. Song, S. Kim, S. Kim, J. Jo, J. P. Baboo, D. T. Pham, D. Y. Putro, Y.-K. Sun, J. Kim, *J. Mater. Chem. A* **2017**, *5*, 23299.
[4] N. Zhang, F. Cheng, J. Liu, L. Wang, X. Long, X. Liu, F. Li, J. Chen, *Nat. Commun.* **2017**, *8*, 405.
[5] M. H. Alfaruqi, V. Mathew, J. Gim, S. Kim, J. Song, J. P. Baboo, S. H. Choi, J. Kim, *Chem. Mater.* **2015**, *27*, 3609.
[6] C. Xu, B. Li, H. Du, F. Kang, *Angew. Chem., Int. Ed.* **2012**, *51*, 933.
[7] M. H. Alfaruqi, J. Gim, S. Kim, J. Song, J. Jo, S. Kim, V. Mathew, J. Kim, *J. Power Sources* **2015**, *288*, 320.
[8] B. Lee, H. R. Lee, H. Kim, K. Y. Chung, B. W. Cho, S. H. Oh, *Chem. Commun.* **2015**, *51*, 9265.
[9] X. Gao, H. Zhang, X. Liu, X. Lu, *Carbon Energy* **2020**, *2*, 387.
[10] X. Guo, J. Li, X. Jin, Y. Han, Y. Lin, S. Wang, L. Qin, S. Jiao, R. Cao, *Nanomaterials* **2018**, *8*, 301.
[11] M. H. Alfaruqi, S. Islam, D. Y. Putro, V. Mathew, S. Kim, J. Jo, S. Kim, Y.-K. Sun, K. Kim, J. Kim, *Electrochim. Acta* **2018**, *276*, 1.
[12] Y. Jin, L. Zou, L. Liu, M. H. Engelhard, R. L. Patel, Z. Nie, K. S. Han, Y. Shao, C. Wang, J. Zhu, H. Pan, J. Liu, *Adv. Mater.* **2019**, *31*, 1900567.
[13] G. Fang, C. Zhu, M. Chen, J. Zhou, B. Tang, X. Cao, X. Zheng, A. Pan, S. Liang, *Adv. Funct. Mater.* **2019**, *29*, 1808375.
[14] J. Hao, J. Mou, J. Zhang, L. Dong, W. Liu, C. Xu, F. Kang, *Electrochim. Acta* **2018**, *259*, 170.
[15] J. Long, F. Yang, J. Cuan, J. Wu, Z. Yang, H. Jiang, R. Song, W. Song, J. Mao, Z. Guo, *ACS Appl. Mater. Interfaces* **2020**, *12*, 32526.
[16] B. Puértolas, A. Smith, I. Vázquez, A. Dejoz, A. Moragues, T. Garcia, B. Solsona, *Chem. Eng. J.* **2013**, *229*, 547.
[17] P. Almodóvar, D. A. Giraldo, J. Chacón, I. Álvarez-Serrano, *ChemElectroChem* **2020**, *7*, 2102.
[18] A. C. Gaillot, D. Flot, V. A. Drits, A. Manceau, M. Burghammer, B. Lanson, *Chem. Mater.* **2003**, *15*, 4666.
[19] A. C. Gaillot, V. A. Drits, A. Plancuon, B. Lanson, *Chem. Mater.* **2004**, *16*, 1890.
[20] L. D. Kulish, P. Nukala, R. Scholtens, A. G. M. Uiterwijk, R. Hamming-Green, G. R. Blake, *J. Mater. Chem. C* **2021**, *9*, 1370.
[21] N. P. Arias, M. E. Becerra, O. Giraldo, *Nanomaterials* **2019**, *9*, 1156.
[22] M. E. Becerra, N. P. Arias, O. H. Giraldo, F. E. López, M. J. Illán Gómez, A. Bueno, *Appl. Catal., B* **2011**, *102*, 260.
[23] Y. Li, S. Wang, J. R. Salvador, J. Wu, B. Liu, W. Yang, J. Yang, W. Zhang, J. Liu, J. Yang, *Chem. Mater.* **2019**, *31*, 2036.
[24] W. Sun, F. Wang, S. Hou, C. Yang, X. Fan, Z. Ma, T, G., F. Han, R. Hu, M. Zhu, C. Wan, *J. Am. Chem. Soc.* **2017**, *139*, 9775.
[25] D. Chao, W. Zhou, C. Ye, Q. Zhang, Y. Chen, L. Gu, K. Davey, S.-Z. Qiao, *Angew. Chem., Int. Ed.* **2019**, *58*, 7823.
[26] X. Guo, J. Zhou, C. Bai, X. Li, G. Fang, S. Liang, *Mater. Today Energy* **2020**, *16*, 100396.
[27] X. Chen, W. Li, Z. Zeng, D. Reed, X. Li, X. Liu, *Chem. Eng. J.* **2021**, *405*, 126969.
[28] X. Shen, X. Wang, Y. Zhou, Y. Shi, L. Zhao, H. Jin, J. Di, Q. Li, *Adv. Funct. Mater.* **2021**, *31*, 2101579.
[29] W. Zhang, X. Zhai, Y. Zhang, H. Wei, J. Ma, J. Wang, L. Liang, Y. Liu, G. Wang, F. Ren, S. Wei, *Front. Energy Res.* **2020**, *8*, 195.
[30] Y. Jiang, D. Ba, Y. Li, J. Liu, *Adv. Sci.* **2020**, *7*, 1902795.
[31] A. Dhiman, D. G. Ivey, *Batteries Supercaps* **2020**, *3*, 293.
[32] J. Wang, J.-G. Wang, H. Liu, C. Wei, F. Kang, *J. Mater. Chem. A* **2019**, *7*, 13727.
[33] L. Chen, Z. Yang, F. Cui, J. Meng, Y. Jiang, J. Long, X. Zeng, *Mater. Chem. Front.* **2020**, *4*, 213.
[34] S. Yang, M. Zhang, X. Wu, X. Wu, F. Zeng, Y. Li, S. Duan, D. Fan, Y. Yang, X. Wu, *J. Electroanal. Chem.* **2019**, *832*, 69.
[35] X. Fan, Y. Zhu, C. Luo, L. Suo, Y. Lin, T. Gao, K. Xu, C. Wang, *ACS Nano* **2016**, *10*, 5567.
[36] H. M. Rietveld, *J. Appl. Crystallogr.* **1969**, *2*, 65.
[37] J. Rodriguez-Carvajal, *Phys. B* **1993**, *192*, 55.

© 2022 Wiley-VCH GmbH